stellarator news

Published by Fusion Energy Division, Oak Ridge National Laboratory
Building 9201-2 P.O. Box 2009 Oak Ridge, TN 37831-8071, USA

Editor: James A. Rome Issue 65 September 1999
E-Mail: jar@ornl.gov Phone (423) 574-1306 Fax: (423) 576-3647
On the Web at *http://www.ornl.gov/fed/stelnews*

HSX first plasma

First plasma was produced in the Helically Symmetric Experiment (HSX) device on August 31, 1999, at 5:15 PM at the University of Wisconsin HSX Plasma Laboratory. This was a momentous occasion for those involved in the years of design, fabrication and assembly of this 48-modular-coil, quasihelically symmetric optimized stellarator. Final vacuum vessel welding and cleaning had occurred several weeks earlier, and first plasma followed completion of the final coil bus work installation, power supply check-out and testing, and gas feed. This first plasma (Fig. 1) was produced in hydrogen using 1 kW of 2.45-GHz rf

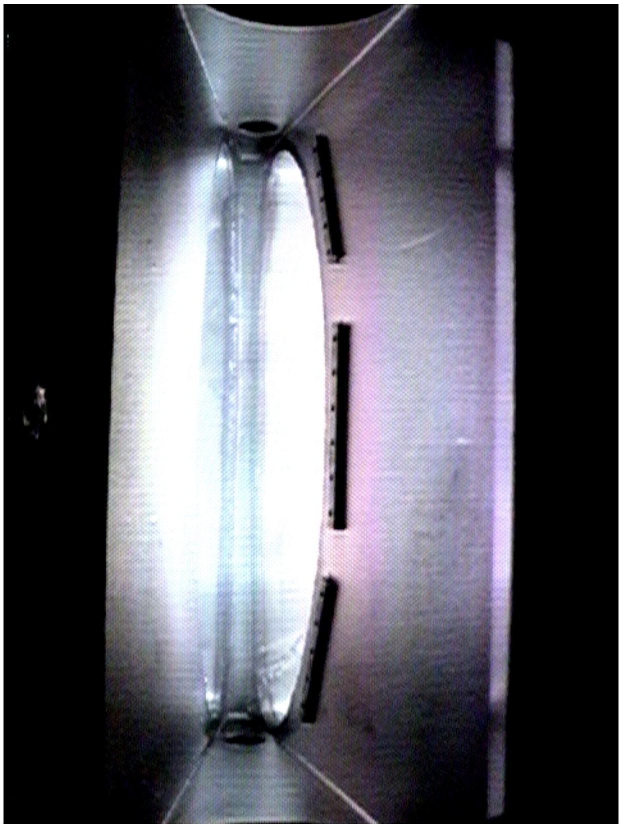

Fig. 1. The first discharge in HSX as viewed through one of the ports.

In this issue . . .

power at a 0.1-T field; this is 10% of the operational field for which HSX was designed. Operation at 0.5- and 1- T is awaiting the last steps in implementing the 28-GHz, 200-kW gyrotron, with its supply and controls, and is anticipated later this year. A photograph of the completed HSX device is shown in Fig. 2.

The initial experiment planned for HSX is electron beam mapping of the magnetic surfaces, with a check-out of the magnetic flexibility inherent in the HSX design. The method chosen for the mapping uses a highly transparent fluorescent mesh which shows the toroidal transits of a low-energy electron beam. The images of this fluorescent mesh are stored digitally and compared to the theoretical HSX magnetic surface shape, quality, and rotational transform.

Magnetic surface mapping experiments were begun shortly after the creation of first plasma in HSX. Early results show nested well-formed surfaces for the base HSX configuration with no evidence of internal magnetic islands. The known 8/7 islands outside of the nominal plasma edge (ɨ = 1.14) were evident. Efforts to refine and analyze these results, and extend the mapping to alternate operational configurations in HSX are underway.

Simon Anderson for the HSX group
Torsatron Stellarator Laboratory
1415 Engineering Drive
University of Wisconsin
Madison, WI 53706
E-mail: fsanders@facstaff.wisc.edu

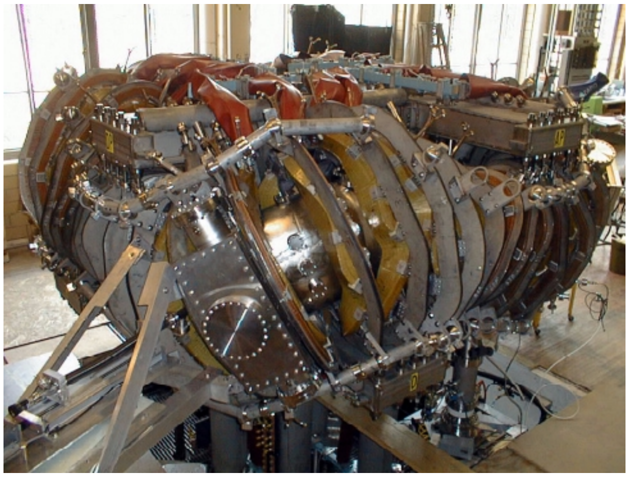

Fig. 2. A view of the completed HSX stellarator.

Fast-ion losses in W7-AS

Good confinement of energetic ions is essential in order to achieve high efficiencies for both auxiliary heating and fusion-born alpha particle heating. The investigation of fast ion losses in stellarators is important, since these configurations suffer from poor confinement of energetic trapped ions because of magnetic field ripple. Such losses can be reduced in optimized field configurations, e.g., in drift-optimized (W7-X) or quasiomnigeneous stellarators. However, fast ions can also be lost when they interact with MHD modes, which can be destabilized by neutral beam injection (NBI) or by fusion-born alpha particles.

The objective of this work is the investigation of fast ion losses in W7-AS, where losses due to NBI, ion cyclotron heating (ICH), and MHD activity are of special interest. Alpha particle losses, in the case of W7-AS, are not relevant since the gyroradius of alpha particles is on the order of the minor plasma radius and these particles are lost immediately.

Fast ion losses were examined with a scintillator-based probe similar to a probe on the Compact Helical System (CHS) [1]. The probe which was designed for the detection of fast ions typically produced by auxiliary heating, can resolve the loss distribution in gyroradius and pitch angle. In addition, the probe can be used as a Faraday cup, supporting quantitative analysis of fast ion losses by a simple current measurement. A new feature of this probe is the simultaneous observation of co- and counter-going ion losses.

We briefly describe the probe and discuss how a reasonable location of the probe at the machine was obtained. Then we present some typical results from experiments with perpendicular and tangential NBI and with minority ICH heating. Finally, an example of MHD-induced losses is shown.

The principle of the probe

The probe consists primarily of two collimator apertures (front aperture: 0.6 mm × 1 mm), which are integrated in the casing of the probe, and a scintillator plate made up of a glass substrate, a metal layer for the current measurement, and segmented scintillator powder (ZnS). The probe head is mounted on a shaft driven by a manipulator, allowing linear motion of the probe head.

This setup works like a magnetic spectrometer, as depicted in Fig. 1. The gyrating ions must pass the apertures before they can strike the scintillator plate. Thus the orbit is characterized by three points defined by the locations of the apertures and the induced light spot. Points 1, 2, and 3 define the gyroradius $R_{\mathrm{g},}$ and points 1 and 3 define the pitch angle $\vartheta_p = \cos^{-1}(v_\parallel/v)$. Instead of using the real gyroradius of the ions, we use $R_g = (2mE_{\mathrm{kin}})^{1/2}/qB$, which is a measure of the kinetic energy.

The velocity distribution of the lost ions is now transformed into a spatial distribution on the scintillator plate. By observing the strike points with an image-intensified CCD camera through an imaging system integrated into the probe shaft, we obtain the distribution of lost ions. In order to get temporal information about the ion losses with sufficient resolution — the maximum frame rate of the CCD system is around 13 Hz — the scintillator light is also guided via a beam splitter and optical fibers to 15 photomultiplier tubes looking at different locations on the scintillator plate. These signals are usually sampled at 4 kHz.

As mentioned above, co- and counter-going ion losses can be measured simultaneously. This is accomplished by arranging two collimators so that the resulting distributions of co- and counter-ions are staggered without significant overlap. Figure 2 shows a top view of the scintillator, meshes of calculated coordinate systems (R_g, ϑ_p), and the approximate locations observed by the photomultipliers. The scintillator and the metal layer are divided in two parts by an insulating strip allowing a current measurement of co- and counter-ions independently.

The calculation of the coordinates, necessary for a transformation of the loss distribution into rectangular coordinates, was performed with a Monte Carlo orbit simulation using the exact geometry of the probe head from computer aided design (CAD) data and an orbit integration in vacuum magnetic fields. In general, these grids have to be calculated for every field configuration and probe position, but the resulting variations are rather small.

Location of the probe and expected fast ion losses

W7-AS is divided into five periods, in which the plasma cross section varies from elliptical at φ = 36° to triangular at φ = 0°. The location of the probe was chosen so that losses of passing and trapped particles can be detected. Losses of passing particles mean that the drift orbits have large excursions and a scraping off can occur eventually at the probe head. Such losses can, in principle, be measured at any position depending on the deviation of drift surfaces from flux surfaces. For trapped particles, however, the probe has to be placed in a local minimum of B_{mod}. The ∇B ion drift under normal operating conditions in W7-AS is upward; thus, the probe is mounted on top of the machine in the φ = 27° plane. The correct location of the probe was also checked with strike point patterns obtained by the FAFNER code [2] and an orbit code developed for this work.

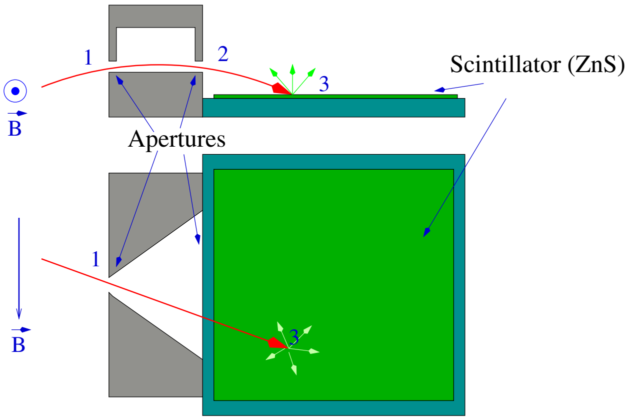

Fig. 1. The principle of the probe.

Figure 3 demonstrates how trapped particles may enter the probe with two guiding center trajectories in magnetic coordinates. Ions are trapped in the local magnetic mirrors and, finally, drift radially outwards to the local mirror located at φ = 18°–30° and $\vartheta_{\mathrm{mag}} = 60°$. These orbits indicate that measured losses may strongly depend on the magnetic field configuration. Here small variations in ∇B lead to different orbits, and in Fig. 3 the ions enter different adjacent periods (the orbit shown in red is for an ion reflected by the stronger gradient at the first stagnation

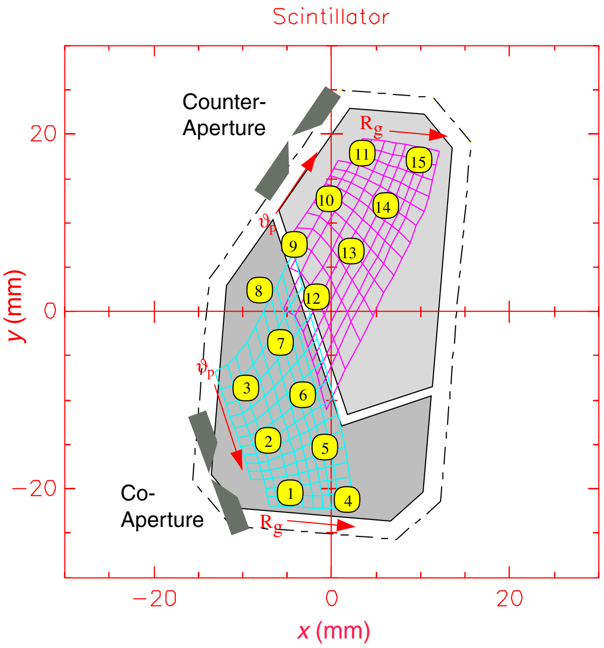

Fig. 2. Outline of the scintillator plate, the locations observed by the 15 photomultipliers, and calculated grids of gyroradius, R_g, and pitch angle, ϑ_p, for co- and counter-going ions.

point and is finally trapped in the same local mirror but in an adjacent period).

In the following, particle losses are classified only as either trapped or passing, since in W7-AS a sharp boundary (trapped and lost/passing) exists in phase space for energetic ions. For thermal ions, this boundary is blurred and banana orbits can also be found. In general, a classification of orbits can not be performed due to the complicated field structure of W7-AS.

Losses with perpendicular NBI—Probe test

The diagnostic neutral beam injector on W7-AS, usually used for charge exchange neutral particle analysis, serves as a test facility for the fast ion probe, because the injector and the probe are located in adjacent half-periods at stellarator symmetric ports. Ideally, ions produced by the diagnostic injector should drift to the probe (e.g., yellow orbit in Fig. 3). Thus it is possible to test whether the observed light patterns result from striking ions or from unfavorable stray light effects.

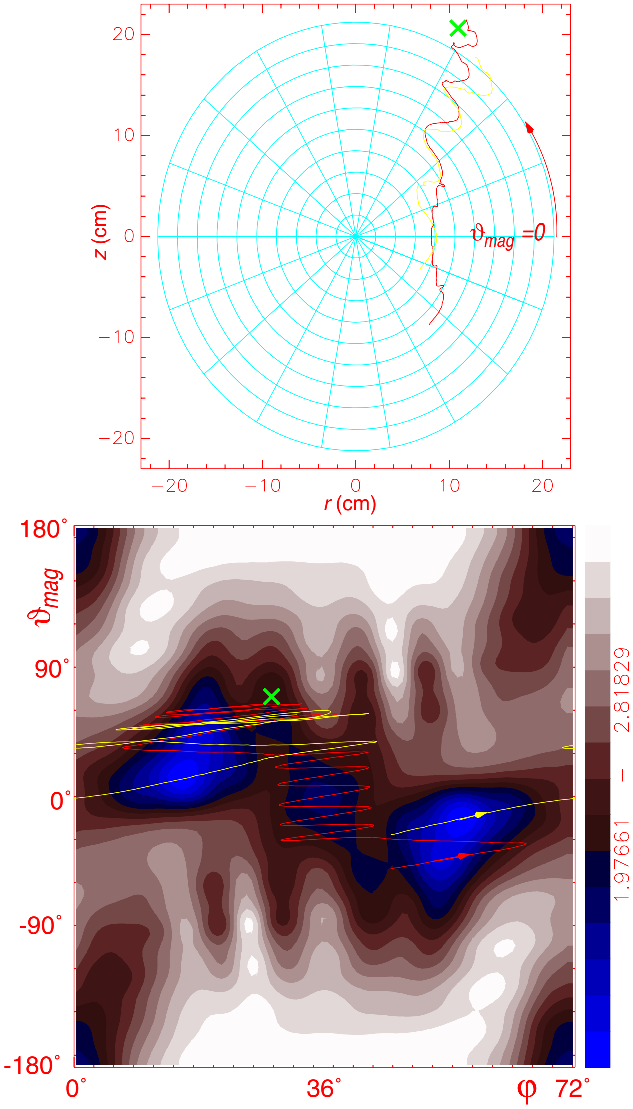

Fig. 3. Orbits of trapped 50-keV hydrogen ions in magnetic coordinates at a pitch angle of 80° for two different starting positions (determined by ion birth points of the diagnostic neutral beam). The location of the probe is indicated by the cross (×). The lower picture shows the B_{mod} surface of one field period at $r_{eff} = 20$ cm.

Results for a discharge with electron cyclotron resonance heating (ECRH) are shown in Fig. 4 which presents some global plasma parameters (plasma stored energy W_{equil}, ECRH power P_{ECRH}, radiated power measured with a bolometer P_{BOLO}, and H_{α}), current signals for the lost

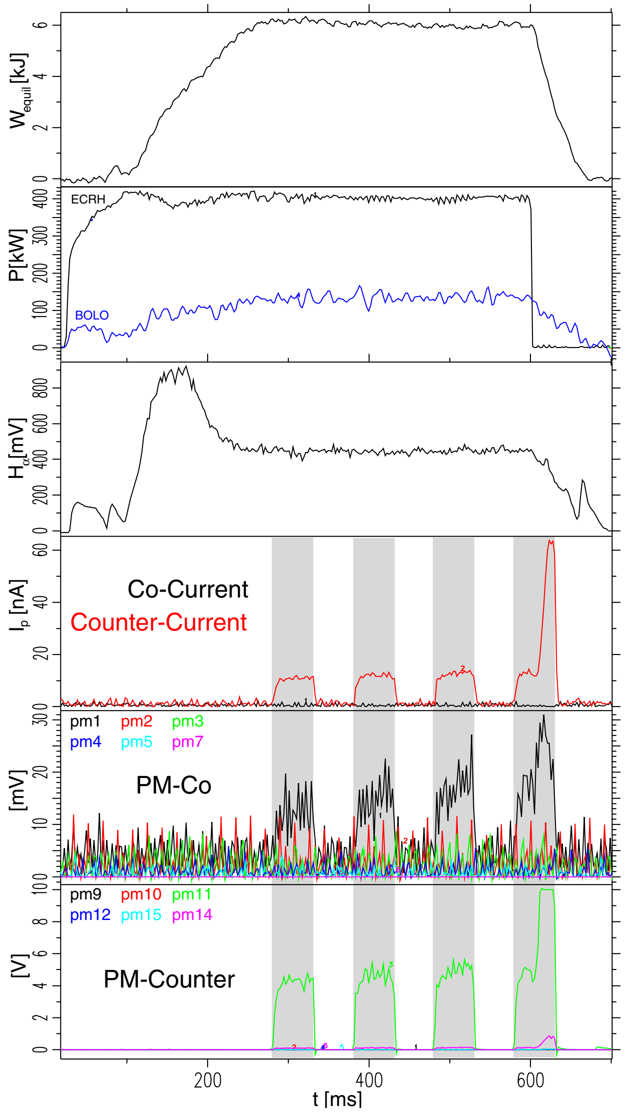

Fig. 4. Time traces of global plasma parameters W_{equil}, P_{ECRH}, P_{BOLO}, and H_{α}, the ion current, and photomultiplier (PM) signals of the fast ion probe for shot #47476. The PM numbers are the same as in Fig. 2. The time intervals of the diagnostic NBI pulses are indicated by the shaded bars.

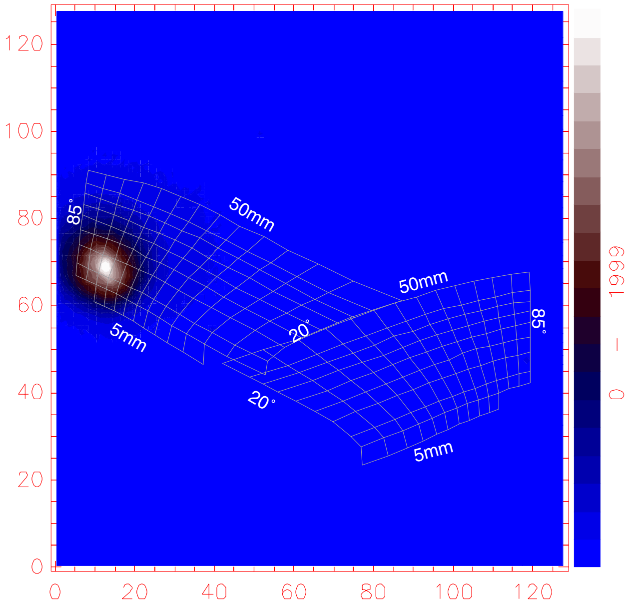

Fig. 5. Image from the CCD chip. Calculated grids with the ranges of pitch angle and gyroradius are also included. The spacing in pitch angle is 5° and the lines of constant R_g are at 5, 7.5, 10, 15, 20, 25, 30, 35, 40, and 50 mm.

ions, and the photomultiplier (PM) signals. The PM signals exhibit ion losses exclusively during NBI. No correlation with H_α signals can be seen. In this example, a mirror field configuration was chosen (enhanced B_{mod} at $\varphi = 36°$) to demonstrate the independent measurement of co- and counter-going fast ions. As expected, losses only occur at large pitch angles. Losses of co-going ions, however, are strongly suppressed by the steep gradient of B_{mod} at the probe position. Without a magnetic mirror field, losses of both co- and counter-going ions have nearly the same intensity, since the trapped particles bounce in the local magnetic mirror (Fig. 3). Nevertheless, co-losses are often lower than the counter-losses because of a scrapeoff at the top limiter located near the probe (at $\varphi = 36°$).

The corresponding light distribution on the scintillator plate during the injection interval is shown in Fig. 5. The centroid of this distribution is located at pitch angles around 75° and a gyroradius close to 10 mm. The nominal maximum gyroradius of the birth ion is 10.6 mm for this case (34-keV H^+ at $B_{mod} = 2.5$ T). At normal field configuration the equivalent spot also appears on the co side, which enables an alignment check of the calculated grids. The distribution spreads beyond the calculated grid, presumably because of a halo of the scintillator plate.

Losses with tangential NBI

W7-AS is equipped with tangential co- and counter-NBI. We now examine the losses of passing particles by co-injection in a discharge with combined ECH and NBI heating. Figure 6 shows global plasma parameters and the PM signals for this discharge.

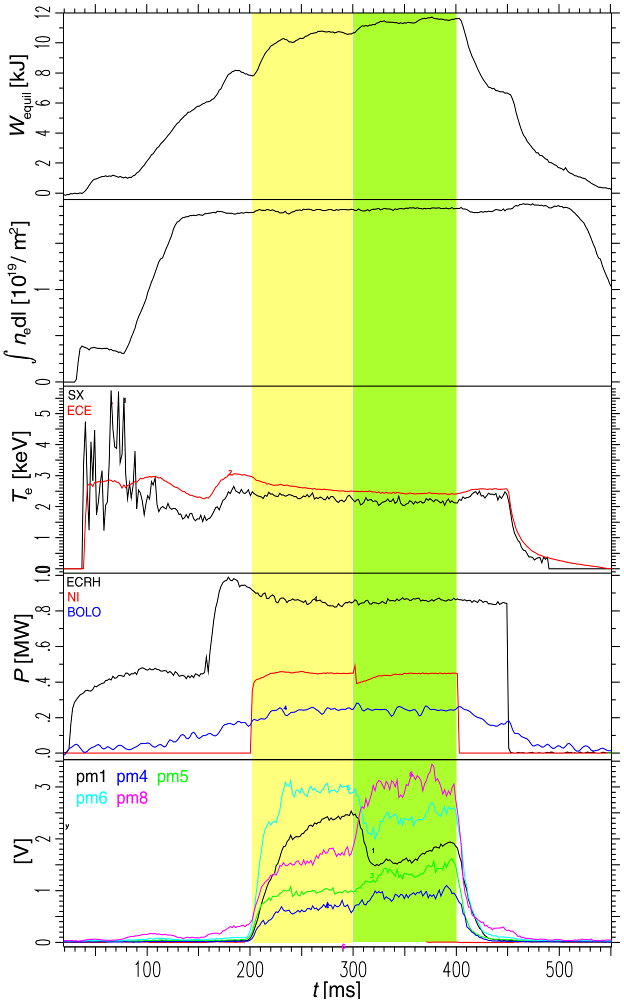

Fig. 6. Results of tangential NBI (200–400 ms) during an ECRH discharge (shot 45965). W_{equil}, line density, central T_e, P_{ECRH} and P_{NBI} as well as PM signals are shown. At 300 ms the beam is switched from an outer to an inner source.

In such discharges, high electron temperatures (here 2.5 keV) are achieved so that the slowing down of the ions is dominated by ion-ion instead of electron-ion collisions. This is confirmed by the critical ion energy, at which the beam ions slow down equally on the plasma ions and electrons. Here, according to Stix [3], this energy roughly amounts to 45 keV. Under these conditions ions can change their momentum before losing kinetic energy; that is, fast ion losses at large pitch angles (PM ch. 1) can be observed although the ions have pitch angles around 30° at birth.

During the NBI phase of this discharge, the beam was switched from an outer to an inner source, causing the average pitch angle of the beam ions to change from 35° to

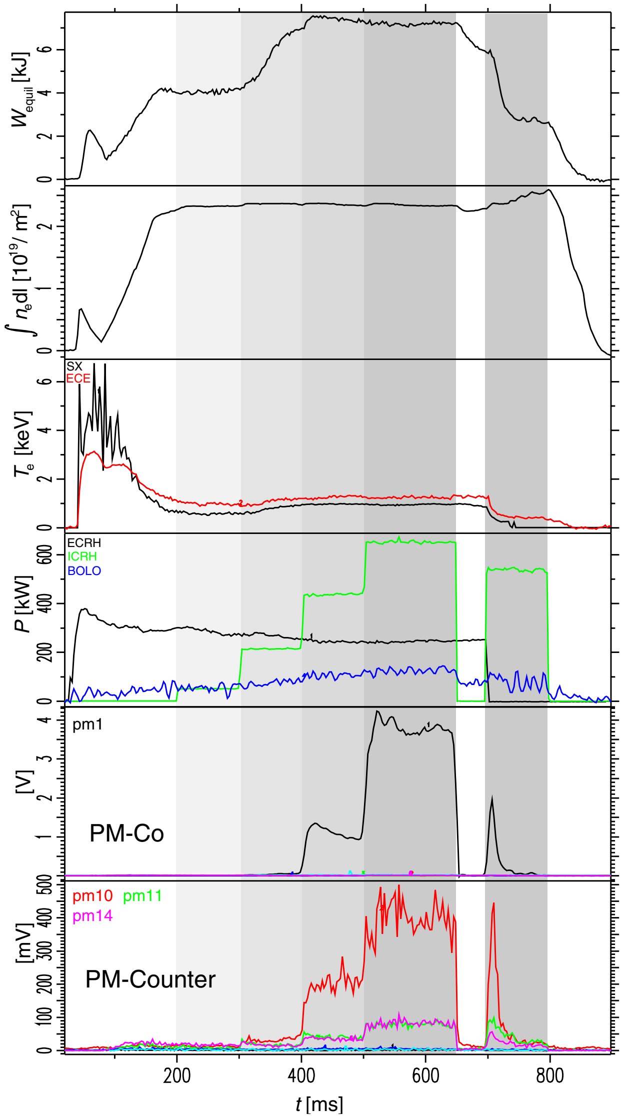

Fig. 7. Results from a discharge (shot 47024) with minority ICRH heating. The plasma stored energy is W_{equil}. Also shown are the line integrated n_e, central T_e, P_{ECRH}, P_{ICRH}, P_{BOLO} and ion loss signals of photomultipliers. The ICRF power is increased in a stepwise fashion beginning at 200 ms.

21°. The PM signals of channel 8 ($\vartheta_p \simeq 15°$) and 6 ($\vartheta_p \simeq 40°$) exhibit opposite behavior over time, indicating that the losses directly reflect the distribution of passing ions. The fraction of trapped ions (PM ch. 1) is also larger for the outer source; a possible explanation is that the distance in phase space of birth ions to the trapped/passing boundary is smaller and less diffusion in pitch angle is necessary to scatter them into the loss cone. The energy signal derived from saddle coils (measuring the Pfirsch-Schlüter current) is increases slightly in the second NBI phase where the losses of trapped particles drop. This energy signal may indicate a change in the parallel energy content due to fast particles from the tangential injection, because the diamagnetic energy signal (not shown here) stays constant during the switching of the NBI sources.

In general, the observed losses due to NBI heating decrease rapidly with lower T_e, as is the case in discharges without ECRH. In density scans with combined heating and with NBI alone, the ratio of trapped to passing particle losses has also been examined. A lower ratio for decreasing T_e and decreasing plasma density is found. The currents measured with our probe are much lower (only 10 nA at 2.5 T) than those observed at CHS ($I_{cup} \simeq$ 500 nA) [1], although the sizes of the apertures are of the same order. Scans in B_{mod} have shown that at 1.0 T the loss currents increase to 100 nA, which is closer to the CHS result. Stronger losses at lower fields can be easily explained in terms of larger deviations of drift surfaces from flux surfaces.

Losses induced with ICH

In W7-AS, ICH is often less efficient than ECRH. The fast ion probe may be an instrument to clarify this issue. Ions accelerated by the launched wave predominantly gain perpendicular momentum, and thus they probably enter or reside in the loss cone of phase space. If the slowing-down time of the ions is long enough, they should drift to the wall instead of dissipating their energy to the plasma. This can be demonstrated by the results shown in Fig. 7, depicting the case in which minority ICH was applied during an ECRH discharge and a power scan was performed.

First, the plasma is created and sustained by ECRH. After 200 ms the ion cyclotron resonant frequency (ICRF) power is increased stepwise. The first power step is very low, and no influence on the plasma is observed. The second step is sufficient to increase the energy content of the plasma substantially. During the third step, W_{equil} changes only slightly, raising the question of where the applied power is lost.

The signals of the fast ion probe reveal by the steep increase of the photomultiplier signals at high pitch angles, that energetic trapped particles leave the plasma, whereas losses of passing particles remain negligible. The largest increase in the loss signal occurs at 500 ms where W_{equil} is not affected at all. At the beginning of the last ICH pulse, the ECRH is switched off and the loss signals drop as T_e decreases. Finally, at lower T_e, ICH is capable of sustaining the plasma, because the slowing-down time is short enough that the energy of the fast ions can be transferred to the plasma. The CCD data, not shown here for the sake of brevity, exhibit tails in the ion distribution function growing in R_g with larger ICRF power. When the ion losses appear (at 400 ms), the distribution is spread over a pitch angle range from 40° to 80°. With increasing power, a tail in the distribution occurs at 80° to larger R_g. Estimates based on the distribution in R_g reveal ion energies on the order of 100 keV.

MHD-induced losses

Losses of fast ions have also been observed during burst-like MHD activity. To investigate the correlation between this activity and ion losses, a selected set of multiplier signals was recorded at a high sample rate (500 kHz). Figure 8 shows Mirnov, ion loss, and soft X-ray signals on a small time scale during an NBI discharge at $B_{mod} = 1.25$ T. Here, the parallel velocity of the beam ions is close to the Alfvén speed so that beam-driven MHD instabilities can occur.

The correlation between the Mirnov signal, the ion loss signal, and the soft X-ray signals is obvious. Bursts in the loss signal were observed only at high pitch angles, where a large background of trapped particle losses was present. During the bursts the loss is 1.5 times larger. Up to now these signatures could not be found in the passing particle losses.

The MHD activity is not fully analyzed yet, but it seems most likely that in this case global Alfvén eigenmodes (GAEs) are present (low magnetic shear). A wavelet analysis exhibits various frequencies during the bursts, the dominant frequency being around 60 kHz. A time lag between the burst activity and the ion losses can also be seen—the decay time of the scintillator is only around 80 µs—which gives rise to the assumption that the MHD activity is the reason for the losses and not only an accompanying feature. Such a delay has also been observed in CHS [4] and was explained with a threshold amplitude of magnetic fluctuations, which become stabilized when fast ions are expelled from the plasma. The upper soft X-ray signal in Fig. 8 reflects the central temperature, which appears to drop with the onset of the ion losses. The lower soft X-ray signal, being sensitive to the edge, indicates increased recombination radiation due to edge cooling.

The exact analysis of the MHD-induced losses and their influence on the W7-AS plasma is still under development.

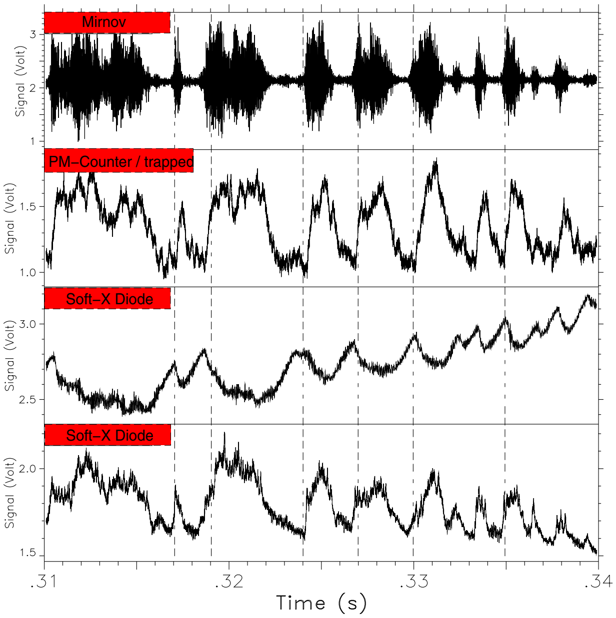

Fig. 8. Mirnov signal, fast ion loss of trapped ions and soft X-ray signals for NBI-driven MHD activity (shot 46535). The upper soft X-ray signal corresponds to an observation close to the plasma center (with filter), the lower to an observation close to the edge (without filter).

Final remark

The escaping fast ion probe gives valuable information about ion losses for various applied heating schemes and different field configurations. Nevertheless, conclusions about the global fast particle confinement must be drawn with caution, since losses are observed only at a single point on the machine. The observed losses depend strongly on the magnetic field configuration, because the optimum probe location varies with the magnetic field structure and the ion scrapeoff by the inner vessel structure changes as well. Therefore, sophisticated calculations are needed in order to compare theoretical and observed losses.

A. Werner, A. Weller, D. S. Darrow,[1] and the W7-AS Team
Max-Planck Institut für Plasmaphysik
EURATOM Association
D-85748 Garching bei München, Germany
[1]Princeton Plasma Physics Laboratory
Princeton, New Jersey 08543

E-mail: andreas.werner@ipp.mpg.de

References

[1] D. S. Darrow et al., Rev. Sci. Instrum. **70**, 838 (1999).

[2] F.-P. Penningsfeld, Europhys. Conf. Abstr.**7D**, 323 (1983).

[3] T. H. Stix, Plasma Phys. **14**, 367 (1972).

[4] M. Isobe, in Europhys. Conf. Abstr. **23J**, 21 (1999).

Study of energetic-ion-driven global instabilities in heliotron/torsatron plasmas

Study of the interaction between energetic or alpha particles and MHD oscillations is a critical issue for a fusion reactor. In large tokamaks, energetic-ion-driven instabilities and their effects on energetic ion confinement have been extensively studied. Recently, significant progress in plasma confinement in helical systems has brought about an opportunity to do research on energetic ion effects in three-dimensional configurations. In the Compact Helical System (CHS) heliotron/torsatron, we have observed two types of characteristic MHD instabilities destabilized by the presence of energetic ions: toroidicity-induced Alfvén eigenmodes (TAEs) and fishbone-like burst modes (FBs) [1, 2]. Here, we report characteristics of the energetic-ion-driven MHD instabilities observed in CHS.

In CHS, both TAEs and FBs are often observed in a relatively low-density regime ($n_e \le 3 \times 10^{19}\,\mathrm{m}^{-3}$) at low toroidal field ($B_t = 0.75$–1.5 T) during tangential co-neutral beam injection (NBI), where the injection energy of the hydrogen beams is 34–40 keV. In these plasmas, the average (parallel) beta of the energetic beam ions is in the range 0.1–0.3% and is comparable to the bulk plasma beta. Figure 1 shows the time evolution of coherent magnetic fluctuations of TAEs in the NBI-heated plasma. The toroidal mode numbers of the two coherent modes seen in Fig. 1 are $n = 1$ and 2. Their frequencies decrease in time with increasing electron density n_e, exhibiting a dependence of $1/(n_e)^{1/2}$ and are about 70% of the predicted TAE gap frequency $f_{TAE} = V_A/4\pi Rq$, where V_A, R, and $1/q$ are the Alfvén velocity, the plasma major radius, and the rotational transform, respectively.

In Fig. 2, the frequencies observed for various n_e and B_t are plotted as a function of the TAE gap frequency. The observed frequencies clearly scale well with f_{TAE}. The difference of about 30% between the observed frequencies and f_{TAE} can be explained by the presence of impurity ions and the TAE gap width. The effect of toroidal plasma rotation on the observed frequencies is very small, less than 6 kHz even for $n = 2$. The results in Figs. 1 and 2 suggest that these modes are TAEs destabilized by injected energetic beam ions. Calculation of the TAE gap structure in the three-dimensional configuration of CHS is fairly complicated. Here, the TAE gap structure was calculated by a simple dispersion relation for a large-aspect-ratio tokamak equilibrium [3].

The expression for the TAE (full) gap width includes the effect of helical ripple and is $2\Delta f \sim 2(\varepsilon_t + \varepsilon_h + \Delta')$, where ε_h is the helical ripple, ε_t is the toroidal ripple ($\sim \langle r \rangle / R$), and

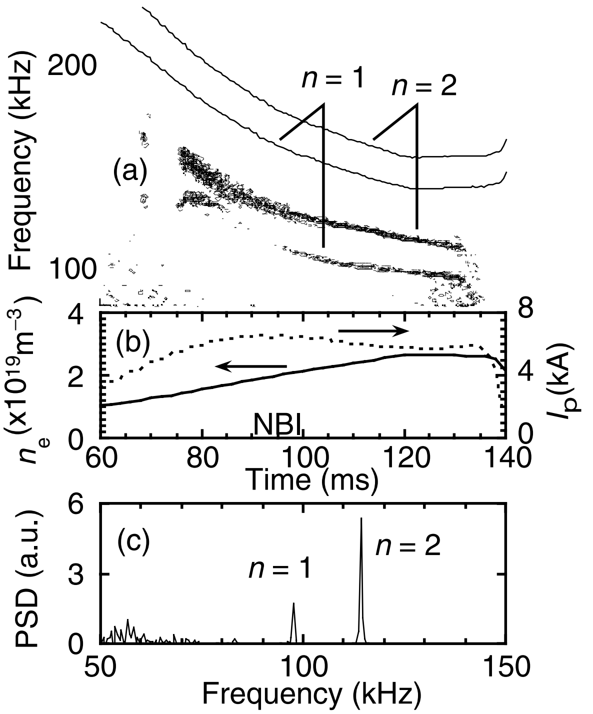

Fig. 1. Time evolution of TAEs in a co-NBI-heated plasma. (a) Contour plot of magnetic fluctuation intensity as a function of frequency and time. Solid curves show the calculated TAE gap frequency for a pure hydrogen plasma. (b) Electron density and plasma current vs time. (c) Spectral power density for the magnetic fluctuations ($t = 120$–122 ms).

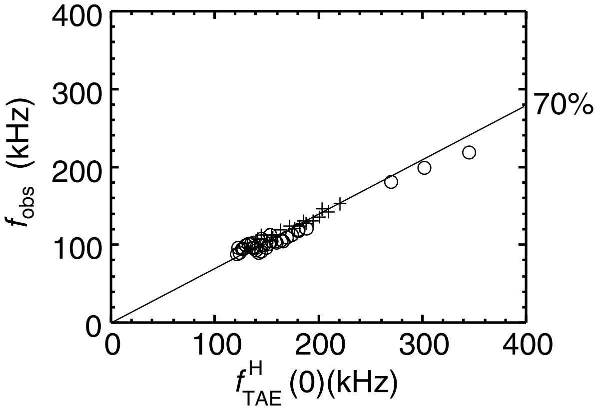

Fig. 2. Comparison of the observed TAE frequency with the TAE gap frequency calculated at the plasma center for a pure hydrogen plasma, where the q value is calculated as $q = (m + 1/2)/n$. Open circles indicate the $n = 1$ mode and plus signs the $n = 2$ mode.

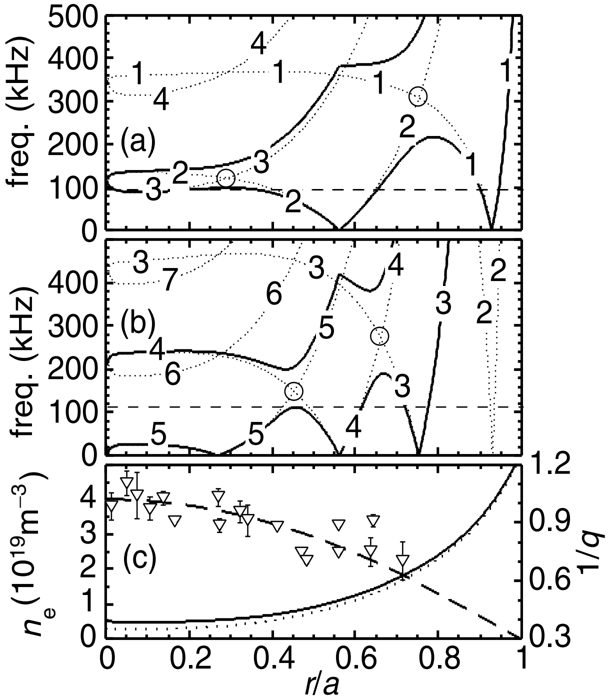

Fig. 3. TAE gap structures, electron density, and rotational transform for the co-NBI-heated plasma of Fig. 1 at 120 ms. (a) Shear Alfvén continua in cylindrical geometry (dotted curve) for the $n = 1$ mode, with the presence of impurity ions taken into account. The Alfvén continua are labeled by the respective m. Open circles indicate the TAE gaps; thick curves show the calculated TAE gaps. The horizontal broken line indicates the observed frequency. (b) Results for the $n = 2$ mode. (c) Rotational transform profile (solid) and density (dotted) in the case without observation of TAEs.

Δ' is the radial derivative of the Shafranov shift. Under experimental conditions, $2\Delta f$ is determined by ε_t and Δ' in the plasma core region (normalized minor radius $\rho < 0.7$).

Figure 3 shows the TAE gap structures calculated with the simplified model for $n = 1$ and $n = 2$ modes. Here, the rotational transform profile $1/q$ is derived as the sum of the rotational transform due to the net plasma current induced by co-NBI and the external rotational transform in a three-dimensional current-free equilibrium with the average bulk beta of 0.2%. The plasma mass density is enhanced by a factor of 1.4 to simulate the presence of impurity ions. As seen in Fig. 3, the observed frequencies of $n = 1$ and $n = 2$ modes lie near the lower bound of the innermost TAE gap. The observed TAE frequency always intersects the shear Alfvén continua in the plasma edge region; this is caused by the characteristic profile of the rotational transform in a heliotron/torsatron plasma. In this situation, TAEs may be stabilized by strong continuum damping near the edge region with high magnetic shear. However, if the TAEs were localized in the plasma core region with low magnetic shear, they would be destabilized by the presence of energetic ions. The internal structure of TAEs was measured with the soft X-ray (SX) fan array of 20 channels and a heavy ion beam probe. The measured results clearly showed that the TAEs are localized around the plasma core region, $\rho \sim 0.2$–0.6. This is consistent with Fig. 3. In CHS, TAE fluctuations are excited well above the noise level of the magnetic probe, only when the velocity of the tangentially injected beam V_b exceeds about half of the central Alfvén velocity $V_A(0)$ and when the net plasma current induced by co-NBI is in the required range. The former requirement suggests side-band excitation where $V_b/V_A(0) \sim 1/3$. The latter implies that the magnetic shear in the plasma core is appreciably reduced by the plasma current induced by co-NBI.

In the region of reduced magnetic shear at the plasma core, the so-called core-localized TAEs observed in a tokamak plasma would be more unstable [4]. The observed internal structure of TAEs in CHS is similar to the core-localized TAEs, which would be unstable without strong continuum damping near the plasma edge. So far, no enhanced energetic ion loss caused by TAEs has been detected with an escaping ion probe. This may be because of low fluctuation amplitude, limited space coverage of the escaping ion probe, or redistribution of the energetic ion profile. The effects of the three-dimensional configuration on the TAE gap structure are under investigation.

Other types of global instabilities destabilized by energetic ions are also observed in CHS, having a character similar to the fishbone instabilities in a tokamak plasma [5]. That is, the time evolution of the magnetic fluctuations has fishbone-like amplitude modulation, and a strong whistling down of the frequency takes place during each burst. They have the mode numbers $m = 2/n = 1$ and $m = 3/n = 2$ in contrast to the $m = 1/n = 1$ fishbone instabilities in a tokamak plasma. Moreover, the instability most likely excited by energetic ions is the ideal resistive interchange instability, whereas the internal kink mode plays a crucial role in fishbone instabilities in a tokamak plasma. In CHS, $m = 2/n = 1$ FBs are observed in the so-called "inward-shifted" plasma and $m = 3/n = 2$ FBs in the "outward-shifted" one.

Figure 4 shows an example of $m = 3/n = 2$ FBs. Magnetic fluctuations exhibit fishbone-like amplitude modulation. The loss flux of energetic ions, measured by the escaping ion probe, is transiently enhanced, correlating with each magnetic burst. On the other hand, as shown in Fig. 5, $m = 2/n = 1$ FBs in the latter half of the discharge induce a sawtooth crash in soft X-ray emission, although obvious energetic ion loss is not detected by the ion probe. As mentioned above, the frequency of fishbone fluctuations is whistled down during each burst. Figure 6 shows the time evolution of magnetic fluctuation amplitude and frequency of $m = 2/n = 1$ FBs, where the mode propagates in the dia-

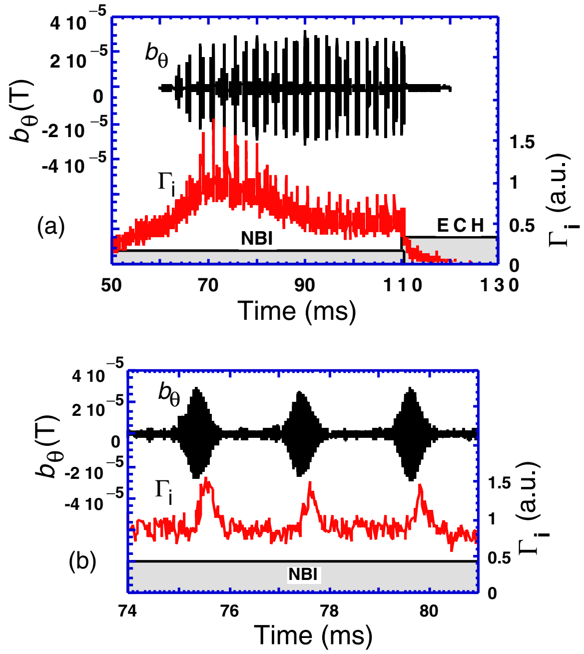

Fig. 4. Top: Time evolution of magnetic fluctuations of $m = 3/n = 2$ FBs and energetic ion loss flux in the outward shifted plasma ($R_{ax} \sim 0.97$ m), where $B_t = 0.9$ T, line averaged electron density ~ 0.8 x 10^{19} m^{-3}, and peak plasma current ~6 kA. Bottom: Expanded time trace.

magnetic drift direction of the energetic ions. This frequency sweep is also a characteristic feature of energetic ion-driven instabilities. The fluctuation amplitude of $m = 3/n = 2$ and $m = 2/n = 1$ FBs has a peak slightly inside the predicted mode rational surface $1/q = 2/3$ or $1/q = 1/2$. In CHS, neutral beams are injected tangentially; that is, the injection angle with respect to the toroidal field is fairly small in the plasma core region (about 19°).

Because of low electron temperature ($T_{e0} < 0.4$ keV), injected beams ($E_b \sim 34$–40 keV) are dominantly slowed down through bulk electron drag without substantial pitch angle scattering. It is predicted that most of the injected energetic ions would not be trapped in helical or toroidal ripple**.** Therefore, the FBs in CHS may be excited by energetic circulating ions, in contrast to the case of the fishbone instability in a tokamak where energetic trapped ions (banana ions) play an essential role in exciting the instability. In Fig. 7, we show a particular shot where both instabilities, FBs and TAEs, are excited. The interesting point is that the growth of the high-frequency part of the $m = 2/n = 1$ FBs about every 2 ms reduces the TAE amplitude. This suggests that the FBs may considerably reduce the beta value of energetic circulating ions and/or the spatial gradient and stabilize the TAEs. If the threshold of excitation for FBs were higher than that for TAEs, the amplitude of FBs would be modulated to be fishbone like. We are now

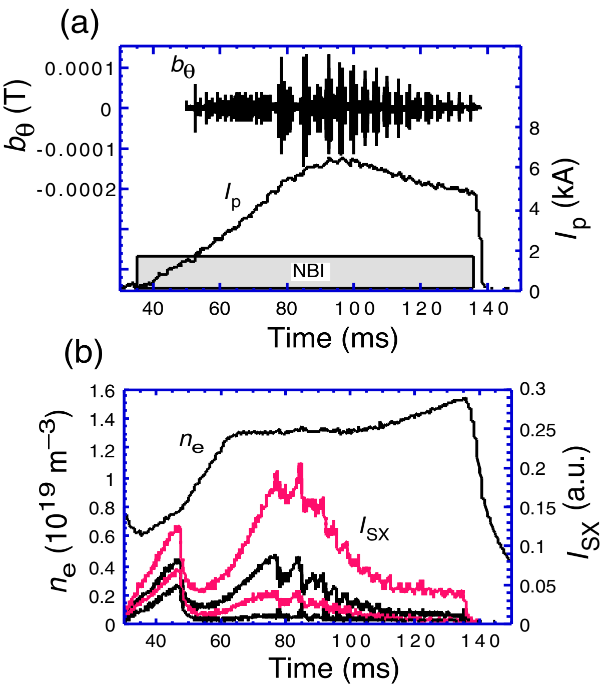

Fig. 5. (a) Time evolution of magnetic fluctuations of $m = 2/n = 1$ FBs in the inward shifted plasma ($R_{ax} \sim 0.92$ m) at $B_t = 0.9$ T. (b) Sawtooth crashes induced by $m = 2/n = 1$ FBs observed in the SX signals.

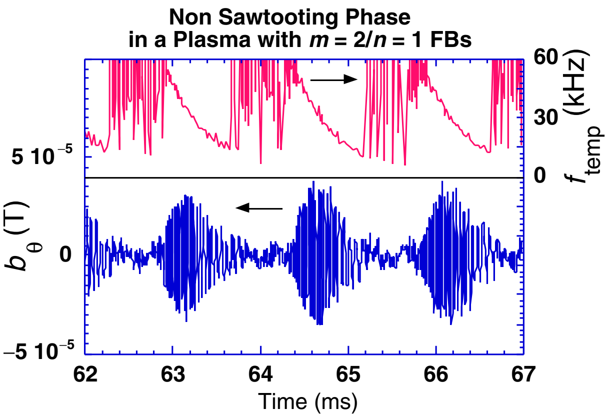

Fig. 6. Detailed behavior of magnetic fluctuations of $m = 2/n = 1$ FBs and the temporal frequency.

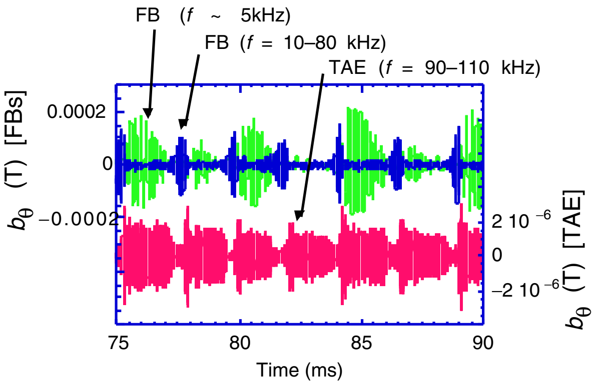

Fig. 7. Time evolution of magnetic fluctuations related to $m = 2/n = 1$ FBs and $m \sim 2/n = 1$ TAEs, where both instabilities are excited in the same shot. FBs consist of two distinct frequency parts. One is a low-frequency part (~ –5 kHz, propagation in the electron diamagnetic drift direction); the other is a high frequency one (10–80 kHz, propagation in the ion diamagnetic drift direction) and results from the frequency sweep during each burst.

studying the detailed mechanisms of excitation of FBs and interaction with TAEs. Moreover, we are extending this research to reactor-relevant high-temperature plasmas in the Large Helical Device (LHD) where intense neutral hydrogen beams with high energy (up to 180 keV) are injected.

Kazuo Toi for the CHS group
National Institute for Fusion Science
Toki, Japan

E-mail: toi@nifs.ac.jp

References

[1] M. Takechi et al., Phys. Rev. Lett. **83**, 312 (1999).

[2] K. Toi et al., paper IAEA-F1-CN-69/EXP1/19 presented at the 17th IAEA Fusion Energy Conference, Yokohama, 1998 (proceedings to be published in Nucl. Fusion).

[3] C. Z. Cheng and M.S. Chance, Phys. Fluids **29**, 3695 (1986).

[4] G.Y. Fu et al., Phys. Rev. Lett. **75**, 2336 (1995).

[5] K. McGuire et al., Phys. Rev. Lett. **50**, 891 (1983).

Stellarator research at the IPP in Garching

Retrospect and prospect on the occasion of the retirement of Prof. G. Grieger

In 1951 Lyman Spitzer, Jr. —Professor of Astronomy at the Princeton University—proposed the stellarator concept as one of the first schemes to confine a thermonuclear plasma. Since that time the stellarator line has experienced many changes and modifications, and a large variety of experiments has explored the plasma behavior using various heating methods. The main argument in favor of stellarators is their potential as a steady-state fusion reactor, an argument, that is becoming more and more important in current fusion reactor studies. Steady state in stellarators is achieved by generating the magnetic field with external coils alone; the currents in the plasma modify this magnetic field only slightly, and a net toroidal current, which must be maintained by an Ohmic transformer or inductive current drive, does not exist. Therefore, those instabilities which are associated with the toroidal current in tokamaks —tearing modes and disruptive instabilities—do not exist in stellarators.

At the IPP Garching, stellarator experiments have been carried out since 1965. Wendelstein 2-A (major radius 50 cm, plasma radius 5 cm) was the first stellarator with steady-state plasma operation, and it demonstrated that plasma confinement in stellarators can be close to classical and not Bohm-like as was found in the Model C-stellarator at Princeton. Furthermore, this low-shear device already showed how strongly confinement may depend on the topology of magnetic surfaces—a feature which also occurred in the following larger experiments. Wendelstein 2-B was similar in size to Wendelstein 2-A; however, because it was equipped with an Ohmic heating transformer, plasma parameters equivalent to those in tokamaks could be achieved. The first large stellarator, Wendelstein 7-A, went into operation in 1976. This device was still a classical stellarator; it was equipped with two pairs of helical windings and toroidal field coils. However, very soon it was recognized that the concept of helical windings is a dead end and cannot be applied to larger devices or to a fusion reactor. This has led to the concept of modular coils, where the total confining field is generated by one set of nonplanar twisted coils. In 1988, Wendelstein 7-AS went into operation, the first large stellarator with modular coils. Wendelstein 7-AS is an upgraded version of Wendelstein 7-A, which posed some restrictions on the optimization of the plasma with respect to plasma equilibrium and transport.

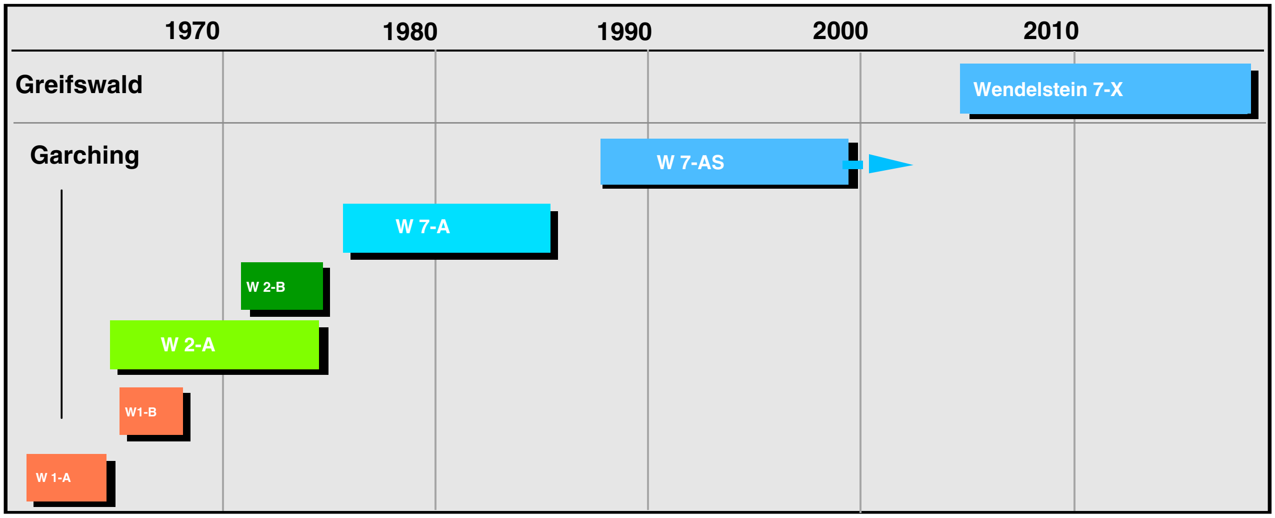

Fig. 1. Time scale of stellarator experiments at the IPP.

In the 10 years from 1976 to 1986, the experiments in Wendelstein 7-A accumulated a large amount of new and interesting results which initiated world-wide interest in the stellarator approach to fusion and have led to the construction of new stellarator devices. Three heating methods were available in W7-A: Ohmic heating (OH), electron cyclotron resonance heating (ECRH) and neutral beam injection (NBI). In particular, experiments without toroidal current and heated solely by ECRH and NBI have demonstrated that in stellarators, plasma parameters comparable to those in tokamaks can be obtained. In 1980, starting with an ohmically-heated plasma, transition to a "currentless" state was achieved by careful control of the rotational transform and shear during the discharge. The buildup of radial electric fields by NBI and the associated poloidal rotation, which led to a significant reduction of ion heat conduction and the improvement of heating efficiency due to improved confinement of injected particles, was recognized. These effects resulted in spectacular plasma parameters with an ion temperature exceeding 1 keV at line averaged densities of $\langle n \rangle = 10^{20}\ \mathrm{m}^{-3}$.

Special attention has been devoted to the effect of the external stellarator field on the induced toroidal current. A major result was the stabilization of the disruptive instability by a sufficiently large stellarator field; in discharges without net toroidal currents both the disruptive instability and tearing mode instability were completely absent.

The Wendelstein 7-AS experiment started in 1988 and is still in operation. A basic feature of this configuration is the reduction of the plasma currents parallel to the magnetic field lines. These so-called Pfirsch-Schlüter currents are the origin of the radial plasma shift with rising plasma pressure, which may become a limiting effect under reactor conditions. The ability to shape the magnetic surfaces through appropriate arrangement of the modular coils

	Wendelstein 7-A	**Wendelstein 7-AS**	**Wendelstein 7-X**
Major radius, m	2	2	5.5
Plasma radius, m	0.09	0.18	0.55
Magnetic field, T	3.4	2.5	3
Rotational transform	0.05–0.6	0. –0.6	0.8–1.2
Coil type	TF + helical windings	Modular	Modular
Conductor	Normal	Normal	SC (NbTi)
Plasma heating	OH, NBI, ECRH	ECRH, ICRH, NBI	ECRH, ICRH, NBI

Table 1. Large stellarators at the IPP

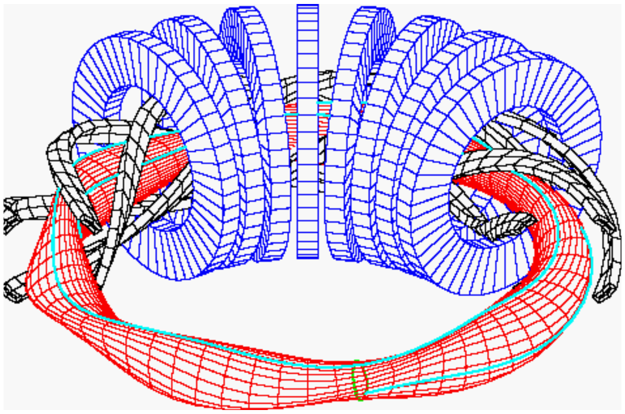

Fig. 2. Schematic of the Wendelstein 7-A stellarator.

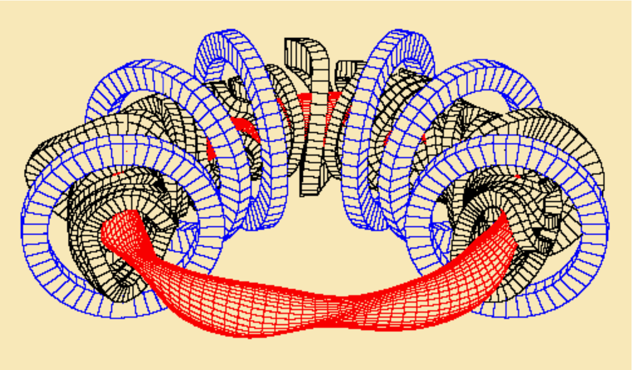

Fig. 3. Coil system and magnetic surface of Wendelstein 7-AS.

made it possible to achieve a special form of the plasma column. Later in the experiment, the efficiency of this concept of optimization was shown: the radial Shafranov shift was found to be a factor of 2 smaller than in the W7-A device. As in W7-A, the absence of the disruptive instability is one of the main features of the experiment. The density limit, which in tokamaks also leads to disruption, is higher than the Greenwald limit and is the result of enhanced impurity radiation. Using ECRH, temperatures up to 6 keV could be reached, and with NBI-heated plasmas, densities up to $n = 2.5 \times 10^{20}$ m^{-3} were achieved. Plasma transport in both Wendelstein experiments is dominated by anomalous processes in the boundary region; in the central region of W7-AS, neoclassical confinement can be reached. Furthermore, H-mode-like confinement was found also in Wendelstein 7-AS and in this context, a strong dependence on the topology of field lines and on the rotational transform has been observed.

Wendelstein 7-AS has demonstrated the viability of the modular coil concept; the experience accumulated with the fabrication and operation of this novel magnet system has prepared the ground for larger stellarator experiments and has increased confidence that even stellarator reactors can make use of this concept. W7-AS is still in operation. The schedule is to focus mainly on divertor studies for better understanding of the physics at the plasma edge.

Pursuing the path of optimization further has resulted in the plan to build a larger stellarator—Wendelstein 7-X—using superconducting (SC) modular coils, with the aim of attaining reactor-relevant plasma parameters. This implies reaching beta values between 4 and 5% and confinement properties, that allow reliable extrapolation towards the reactor regime. The conceptual design of the new experiments began in 1981, and final approval of the project was given in 1996. This Wendelstein 7-X (W7-X) device is presently under construction in the city of Greifswald situated in northeastern Germany, and it is scheduled to begin operation in 2006. Steady-state operation for more than 30 s will demonstrate the reactor potential of this stellarator line, and the envisaged heating power of 10 MW of ECRH and 20 MW of NBI will ensure that plasma temperatures up to 10 keV can be reached. Since plasma-wall interaction will become an important issue in fusion reactors, this topic will be intensively studied in the new experiment. Specially designed divertor target plates will be located at the plasma periphery and will make use of the island geometry in this region.

A large R&D program has been initiated to prepare the technical basis of the device. This implies the development of a NbTi superconducting cable and the construction of a superconducting test coil, which presently is being tested at the FZK in Karlsruhe. Prototype components for the divertor, especially the target elements designed for a power load of 12 $\mathrm{MW/m^2}$, have already been fabricated and successfully tested. The envisaged 10-MW ECH has initiated the development of 140-GHz gyrotrons. The coil system consists of 50 modular coils and 20 planar coils, which are needed to vary the magnetic field and the rotational transform. A test cryostat is under construction to investigate the cooling circuit. Furthermore, a large diagnostic program with international participation is under preparation.

Already during the planning phase of the W7-X experiment, intensive reactor studies have analyzed the basic properties of a stellarator reactor based on the W7-X or Helias concept (Helias = helical advanced stellarator). The size of such a reactor is determined by the need to accommodate a breeding blanket and a shield, by the need to ensure ignition, and by the envisaged fusion power of 3000 MW. The main parameters of this reactor are a major radius of 22 m, and an average plasma radius of 1.8 m. Extrapolating from present confinement data to reactor dimension allows one to operate at low magnetic fields (around 5 T), which is just small enough to allow the use of

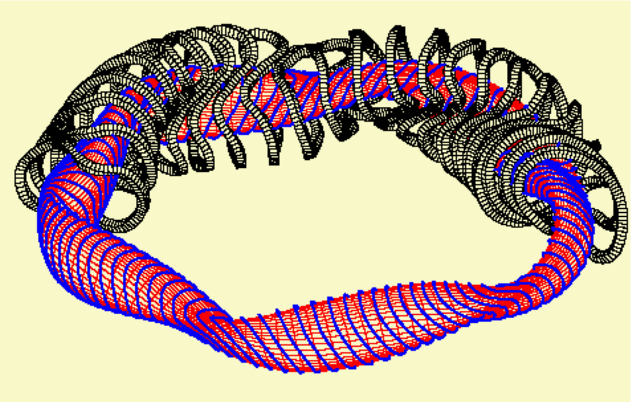

Fig. 4. The Wendelstein 7-X configuration (physicist´s view). Plasma current lines are poloidally closed (solid lines). In some regions current lines and magnetic field lines are almost perpendicular to each other, which is one of the basic features of an optimized or advanced stellarator.

NbTi superconductor. The plasma volume of the stellarator reactor is 1400 m^3 and the area of the first wall is about 2400 m^2; hence the average neutron wall load is on the order of 1 MW/m^2, which is roughly a factor of 2 smaller than in tokamak reactors. Although a stellarator reactor is nonaxisymmetric and therefore poses some problems for maintenance and repair, its inherent potential for steady-state operation, the absence of disruptions, and the low neutron wall load will make it an attractive candidate for a commercial fusion reactor.

Horst Wobig and Hermann Renner

Max-Planck Institut für Plasmaphysik
EURATOM Association
D-85740 Garching bei München, Germany

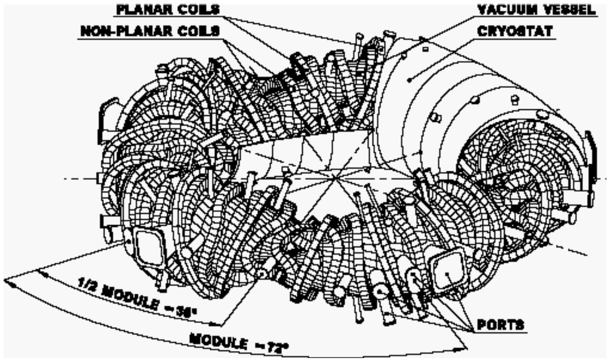

Fig. 5. Wendelstein 7-X coil system, ports, and part of cryostat.

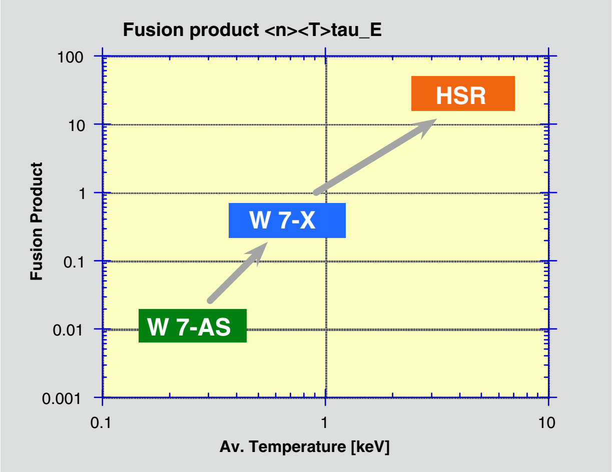

Fig. 6. Fusion product vs average temperature. The figure shows the results attained in W7-AS and those which are expected in W7-X and the Helias reactor (HSR). The extrapolations are made on the basis of empirical scaling laws derived from current stellarator experiments.

Electron density profiles and transport for NBI Plasmas in LHD

Temporal evolutions of electron density profiles have been measured by the 13-channel vertical-view far-infrared (FIR) laser interferometer (CO_2 laser pumped CH_3OH laser, wavelength 118.8 µm) [1, 2] on the Large Helical Device (LHD) [3]. Figure 1 shows the cross section of the interferometer. The beam width is 40 mm in the plasma, and the chord spacing is 90 mm. The FIR interferometer can measure the whole region of plasma including the ergodic region. The electron density at the last closed flux surface (LCFS) sometimes reaches one-third or one-half of the central density. The density approaches zero around the outer boundary of the ergodic region, which is shown as a dashed line in Fig. 1. YAG laser Thomson scattering [4], which measures electron density from X-point to X-point in the horizontal view, confirms this. Contributions from the phase shift caused by the density in the divertor leg are negligible, because the chord at $R = 4.3$ m, which passes through only the divertor legs, shows a negligible phase shift. The simple slice and stack technique is applied for the Abel inversion calculation. The plasma cross section is divided into 10 slices, and the average density of each slice is calculated. Radial density profiles are then constructed from the average density of each slice. Magnetic flux surfaces are calculated from an MHD equilibrium calculation by using the VMEC code, changing the pressure profile and total beta value. Several different magnetic flux surfaces are evaluated to find the equilibrium that minimizes the difference in density between flux surface locations inside and outside the magnetic axis.

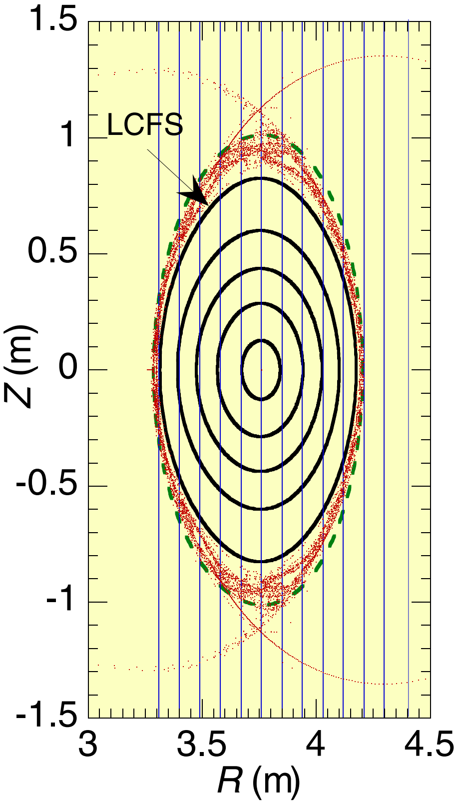

Fig. 1. Cross section of the multichannel interferometer. Thin blue solid lines indicate the interferometer chords. Thick black lines indicate vacuum magnetic surfaces (ρ = 0.2, 0.4, 0.6, 0.8, 1.0) with $R_{ax} = 3.75$ m. Dots indicate the magnetic field line traces in the ergodic and divertor regions.

Here, we concentrate on the comparison of two discharges [1], one with strong density clumping (shot 3560) and one with weak density clumping (shot6616), and characterize both discharges. The two discharges use identical heating (82.6- and 84-GHz ECRH and 3-MW balanced NBI) but different magnetic configurations and toroidal magnetic fields B, the magnetic axis position R_{ax} is at 3.75 m for shot 3560 and at 3.6 m for shot 6616, while B_t is 1.5 T for shot 3560 and 2.5 T for shot 6616. Both are hydrogen discharges. Figure 2 shows the temporal evolution of the line density for shot 3560 (strong density clumping). The line density drops rapidly at $t = 0.5$ s even though NBI and the gas puff continue, and the density profile changes from flat (at $t = 0.5$ s) to hollow (at $t = 0.8$ s), as shown in Fig. 3. In contrast, shot 6616 (weak density clumping) shows a different time history. As shown in Fig. 4, density clumping

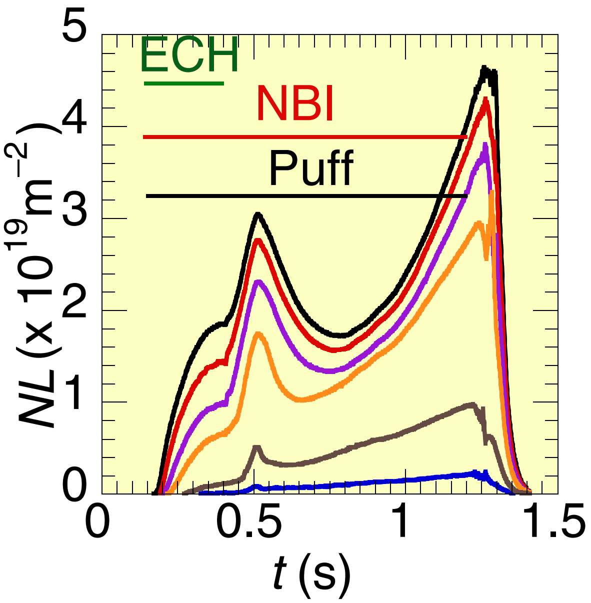

Fig. 2. Measured line density for shot3560 ($R_{ax} = 3.75$ m, $B_t = 1.5$ T, Hydrogen plasma), showing 7 channels of 13.Positions of chords are $R = 3.759$, 3.939, 4.029, 4.209, 4.299,3.399, 3.309 m from the top. Data during a time period $t = 0.5$–0.8 s were used for the analysis.

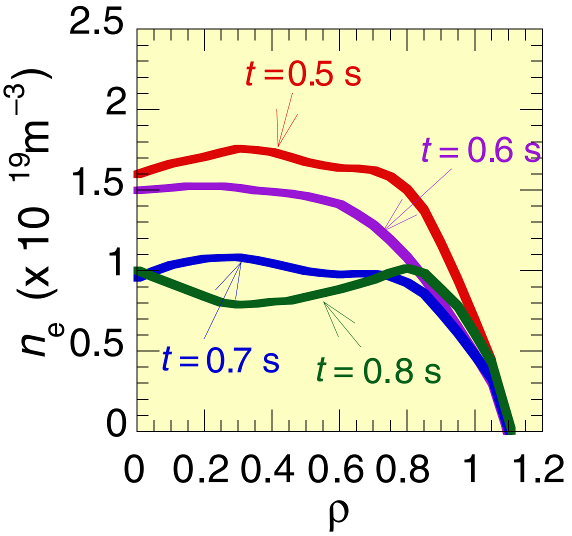

Fig. 3. Radial density profiles for shot 3560.

occurs at $t = 0.5$ s, but it is small at the central chord, and then starts to increase. The density profile changes from hollow (at $t = 0.5$ s) to flat (at $t = 1.0$ s) as shown in Fig. 6. In addition, the H_α intensity from t = 0.5 s to $t = 0.8$ s in shot 3560 (strong density clumping) is about twice the intensity of the one from $t = 0.5$ s to $t = 1.0$ s in shot 6616. This indicates that the particle sources of shot 3560 (strong density clumping) are twice those of shot 6616 (weak density clumping) during these time periods. This simply suggests that particle confinement characteristics are better in the weak density clumping case.

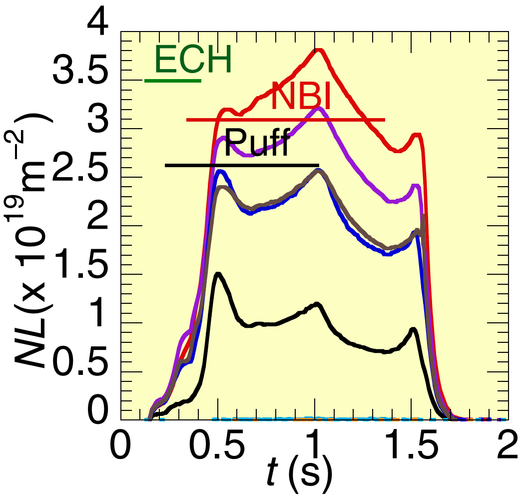

Fig. 4. Measured line density for shot 6616 (R_{ax} = 3.6 m, B_t = 2.5 T, Hydrogen plasma). Channel positions are the same as in Fig. 4. Data during a time period t = 0.5–0.8 s were used for the analysis.

In order to understand the difference of the particle transport quantitatively, correlation of $\nabla n_e/n_e$ and Γ/n_e during the shots was examined. Here, Γ is the particle flux, and it can be calculated from the integral form of the particle-balance equations described by

$$\Gamma(r) = \int_0^r r\left(S - \frac{\partial n_e}{\partial t}\right)dr$$

Here, S is the source rate consisting of beam source (S_{NBI}) and wall source (S_{wall}). Radial profiles of S_{NBI} are calculated from a three-dimensional (3-D) Monte Carlo simulation code [5], and radial profiles of S_{wall} are obtained from a 1-D calculation of rate coefficients of dissociative excitation, ionization, and dissociative recombination of hydrogen molecules [6]. The absolute values of S_{wall} are calculated assuming that the particle confinement time is 0.1 s at $t = 0.5$ s of shot 3560, which is about the same order as the energy confinement time, and S_{wall} multiplies temporal factors so that the line integration of calculated S_{wall} is proportional to the measured H_α intensity. In Fig. 6, the slope of the straight lines, given by the following equation, relates the diffusion coefficients (D) and the y-axis intercept to the convective velocity (V)

$$\Gamma/n_e = -D(\nabla n_e/n_e) + V .$$

In this analysis, data from shot 3560 (strong density clumping) after $t = 0.8$ s were excluded, because the density rise during this time period was caused by an increase of impurity accumulation, making determination of the source profiles more complicated. The data of shot 6616 (weak density clumping) after $t = 1.0$ s were also excluded, because a change of the wall source condition after turning off the gas puffing might affect the transport. Data at ρ = 0.7 were used, because $\nabla n_e/n_e$ changes greatly in both shots at that radius. As shown in Fig. 6, values for the strong density clumping shot (3560) start at the same region as those for the weak density clumping shot (6616).

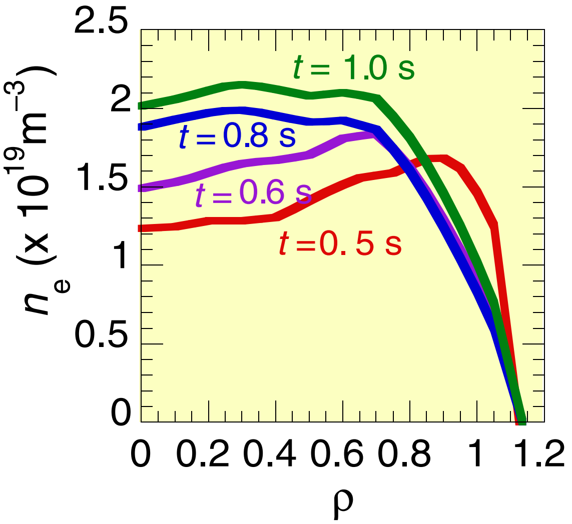

Fig. 5. Radial density profiles for shot 6616.

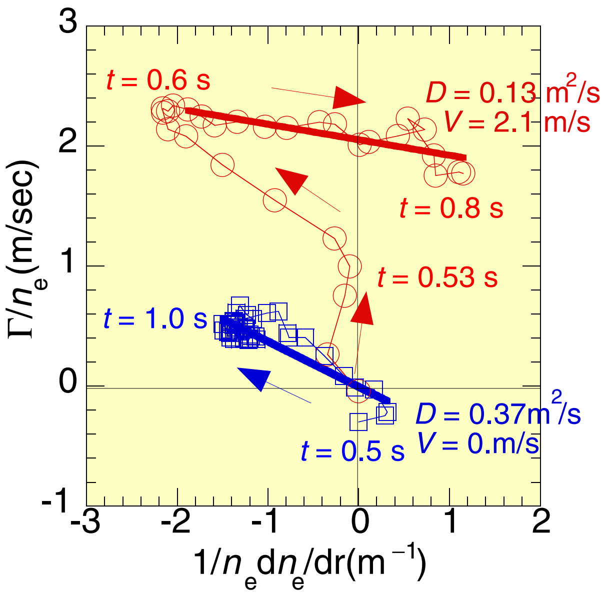

Fig. 6. Γ/n_e vs $(1/n_e)(dn_e/dr)$. Circles indicate shot 3560 (R_{ax} = 3.75 m, B_t = 1.5 T) at ρ = 0.7 for t = 0.5–0.8 s. Squares indicate shot 6616 (R_{ax} = 3.6 m, B_t = 2.5 T) at ρ = 0.7 for t = 0.5–1.0 s. Data points are every 10 ms. Positive Γ indicates outward flux.

However, they transit to different *D*, *V* lines. In both discharges, during the time period t = 0.5–0.6 s, the electron temperature and its gradient at ρ = 0.7 increased rapidly (stronger in shot 3560). This could induce an outward flux, which is predicted by neoclassical theory. From this analysis, *V* is negligible in shot 6616. Smaller *V* can characterize better confinement in shot 6616 (weak density clumping shot) more than a smaller *D*. Although, the analysis is sensitive to the determination of S_{wall}, even if S_{wall} is zero, shot 3560 (strong clumping shot) still needs an outward convective velocity (of about 0.5 m/s) to explain the change of density profiles. At present, it is not certain whether the difference in particle confinement between the two discharges depends on the difference of R_{ax} or B_t. Further experiments and analysis are necessary to find the causality.

K. Tanaka for LHD Experimental Groups
National Institute for Fusion Science
Oroshi 322-6, Toki 509-5292, Japan

Phone: +81-572-2231
Fax: +81-572-58-2624
E-mail: ktanaka@LHD.nifs.ac.jp

References

[1] K. Tanaka et al., in Europhys. Conf. Abstr. **23J**, 1329 (1999).

[2] K. Kawahata, K. Tanaka, Y. Ito, A. Ejiri and S. Okajima, Rev. Sci. Instrum. **70**, 707 (1999).

[3] O. Motojima et al., Phys. Plasmas **6**, 1843 (1999).

[4] K. Narihara et al., to be published.

[5] S. Murakami, N. Nakajima, and M. Okamoto, Trans. Fusion Tech. **27**, 256 (1995).

[6] H. C. Howe, Physics Models in the Toroidal Transport Code PROCTR, ORNL/TM-11521, Oak Ridge National Laboratory (1990).